1   Petrography and geochemistry of carbonate rocks of the Paleoproterozoic Zaonega Formation,

2   Russia: documentation of ^{13}C-depleted non-primary calcite.

3

4   A.E. Črne[a,b], V.A. Melezhik[a], A. Lepland[a,c], A.E. Fallick[d], A.R. Prave[e], A.T. Brasier[d,f]

5

6   [a]Geological Survey of Norway, Postboks 6315 Slupen, NO-7491 Trondheim, Norway;

7   alenka.crne@ngu.no, victor.melezhik@ngu.no, aivo.lepland@ngu.no; tel. +4773904482

8   [b]Ivan Rakovec Institute of Palaeontology ZRC SAZU, Novi trg 2, SI-1000 Ljubljana, Slovenia

9   [c]Tallinn Technical University, Institute of Geology, 19086 Tallinn, Estonia

10   [d]Scottish Universities Environmental Research Centre, Scottish Enterprise Technology Park,

11   East Kilbride G75 0QF, Scotland, UK; aef1p@udcf.gla.ac.uk

12   [e]Department of Earth and Environmental Sciences, University of St Andrews, St Andrews KY16

13   9AL, Scotland, UK; ap13@st-andrews.ac.uk

14   [f]Faculty of Earth and Life Sciences, Vrije Universiteit Amsterdam, De Boelelaan 1085, 1081HV

15   Amsterdam; a.t.brasier@vu.nl

16

17

18   Abstract

19   The ca. 2.0 Ga Zaonega Formation in the Onega Basin of NW Russia represents a deep-water,

20   mixed siliciclastic-carbonate depositional system with voluminous mafic volcanism. It is typified

21   by extremely organic-rich rocks (TOC > 40 wt%) and represents one of the earliest known

22   episodes of oil/asphalt generation. These rocks have been inferred to archive one of the largest

23   negative $\delta^{13}C$ excursions in Earth history, one that followed and/or partially overlapped with the

24   2.2–2.06 Ga worldwide Lomagundi-Jatuli carbonate carbon isotopic excursion to high values

25   and thought to be linked to the Paleoproteorozoic oxygenation of Earth's surface environments.

26   In order to assess the post-depositional integrity of the carbonate carbon isotopic signal

27   ($\delta^{13}C_{carb}$) of the Zaonega rocks, we examined in detail the petrography and geochemistry of eight

28   carbonate beds (0.3 to 0.9 m thick) from different stratigraphic levels of the formation. The range

29   of $\delta^{13}C$ values for a single bed can be as much as 17 ‰, with calcite being significantly depleted

30   in ^{13}C relative to co-existing dolomite; the ^{13}C-depleted calcite likely formed by involvement of

31   carbon derived from diagenetic and catagenetic alteration of organic matter possibly abetted by

32   volcanic CO_2. The presence of calcite ± talc ± phlogopite ± actinolite indicates metamorphic

33   reaction of dolomite with quartz, or possibly K-feldspar, in the presence of water; commonly

34   accompanied by degassing of ^{13}C-enriched CO_2, this caused further ^{13}C depletion of newly

35   formed calcite. The least altered dolomite is documented in central parts of thick dolostone beds

36   with variably calcitized margins. This dolomite is considered as the earliest and possibly primary

37   carbonate phase, potentially recording the $\delta^{13}C$ signal of the ambient seawater. The least-altered

38   dolomite is found in two stratigraphic intervals exhibiting $\delta^{13}C$ values of +8 and +4 ‰ for the

39   middle part of the formation, and $\delta^{13}C$ values of -2 and -4 ‰ for the upper part. All other beds,

40   with $\delta^{13}C$ ranging from -19 to +3 ‰, are considered to have been variably depleted in their [13]C

41   content by post-depositional processes and therefore cannot be reliably used for assessing the

42   carbon isotope composition of Paleoproterozoic seawater. Our results emphasise the importance

43   of distinguishing primary versus secondary (or later) isotopic compositions in studies of

44   carbonate rocks used for reconstruction of global environmental change.

45

46   Keywords: Paleoproteorozoic, carbon cycle, non-primary calcite, Russia, Great Oxidation Event,

47   Onega Basin

48

49   **1. Introduction**

50   Ratios of stable carbon isotopes (^{13}C/^{12}C reported as $\delta^{13}C$) in carbonate rocks are widely

51   used for tracking the global carbon cycle and associated environmental conditions as far back in

52   time as the sedimentary rock record exists (Schidlowski, 2001). One of the most profound events

53   of Earth history was the Paleoproterozoic oxygenation of Earth's atmosphere, beginning around

54   2.5 Ga (Bekker et al., 2004; Farquhar et al., 2000). This is marked by a worldwide $\delta^{13}C$

55   excursion to high values in carbonate rocks (Baker and Fallick, 1989; Karhu and Holland, 1996),

56   and known as the Lomagundi-Jatuli isotopic event. Genesis of this event has been explained by

57   intensive burial of organic matter and associated accumulation of oxygen in the atmosphere

58   (Karhu and Holland, 1996), although Melezhik and Fallick (1996) have discussed some

59   problems with this idea. The Zaonega Formation was deposited after or partially overlapping

60   with the Lomagundi-Jatuli Event (Hannah et al., 2008) and contains rocks extremely enriched in

61 organic matter (TOC > 40 wt%; Melezhik et al., 1999; 2004). The isotopic compositions of

62 reduced and oxidized carbon from the Zaonega Formation have been used in attempts to

63 reconstruct the global carbon cycle for this important interval of Earth history (Kump et al.,

64 2011; Melezhik et al., 1999; Yudovich et al., 1991). The goal of this study is to perform a

65 detailed petrographic and geochemical study of the carbonate-containing rocks of the Zaonega

66 Formation preparatory to an evaluation of their applicability for reconstruction of

67 Paleoproterozoic sea-water compositions, and consequently, for interpretations of perturbations

68 in the global carbon cycle during Paleoproterozoic time.

69   The sedimentary and volcanic rocks of the Zaonega Formation in Karelia, NW Russia

70 (Fig. 1) were drilled as part of the International Continental Drilling Program's Fennoscandia

71 Arctic Russia - Drilling Early Earth Project (FAR-DEEP). The Zaonega rocks record a mixed

72 siliciclastic-carbonate depositional system, with much magmatic activity contemporaneous with

73 sedimentation (Črne et al., 2013a,b). They also contain one of the earliest known generations of

74 oil/asphalt and proposed hydrocarbon seeps onto the sea floor (Melezhik et al., 2009; Qu et al.,

75 2012; Strauss et al., 2013). The Zaonega Formation and associated rocks experienced regional

76 greenschist facies metamorphism during the 1.8 Ga Svecofennian episode of orogenesis

77 (Volodichev, 1987).

78   Previously-reported carbonate δ^{13}C values from the Zaonega Formation range from -25 to

79 +10 ‰ (Krupenik et al., 2011; Kump et al., 2011; Melezhik et al., 1999; Yudovich et al., 1991).

80 Yudovich et al. (1991) interpreted all the ^{13}C-rich carbonate rocks of the Tulomozero and

81 Zaonega formations to be the result of methanogenesis, whereas low δ^{13}C values of the Zaonega

82 carbonates were taken as an indicator of both methanotrophy, and a negative isotopic shift in

83 dissolved inorganic carbon due to atmospheric oxidation of biologically produced CH_4. Krupenik

84 et al. (2011) interpreted all the carbonate rocks to be diagenetically altered to some degree such

85 that the range in carbon isotope values between -1 and -20 ‰ was the result of various

86 proportions of oxidized organic matter being incorporated into early diagenetic carbonate

87 minerals. Most investigations of the Zaonega carbonate rocks highlighted the very low δ^{13}C

88 and/or δ^{18}O values (Krupenik et al., 2011; Melezhik et al., 1999) and/or an exceptionally low

89 Δ^{13}C ($\delta^{13}C_{carbonate}$ - $\delta^{13}C_{organic}$; Kump et al., 2011) to conclude that some post-depositional

90 isotopic overprinting had indeed occurred, but a systematic petrographic and geochemical study

91 to substantiate these inferences has not yet been reported. This paper addresses that shortcoming.

92   The negative $\delta^{13}C$ excursion recorded in the Zaonega Formation, together with assumed

93   coeval strata in the Francevillian Basin, has been interpreted as one of the largest ever

94   perturbations of the global carbon cycle reflecting intense, oxidative weathering of organic-rich

95   rocks as the result of rising oxygen levels in the atmosphere (Kump et al., 2011). This is an

96   important new hypothesis regarding the manner of Earth's transition to an oxygenated planet and

97   underscores the need to carefully assess the potential modification of primary isotopic signals.

98   Post-depositional alteration of the primary $\delta^{13}C$ signal may have occurred during diagenesis

99   driven by respiration of organic matter and also later, during contact and regional metamorphic

100   episodes that the Zaonega rocks have experienced. Within the studied depositional basin, locally

101   generated, syn-sedimentary and/or diagenetic hydrocarbon-rich fluids containing ^{13}C-depleted

102   species, including carbonic acid and CH_4, could have produced secondary carbonates and altered

103   the original carbon isotope composition of primary carbonates. We examined in detail eight

104   representative carbonate beds from cores of the Zaonega Formation, geochemically and

105   petrographically characterizing closely spaced samples within each bed in order to: i)

106   differentiate between early and late carbonate phases and determine their carbon and oxygen

107   isotopic signatures; ii) investigate the potential processes of post-depositional alteration

108   influencing the carbonate carbon isotope record; and iii) estimate the magnitude of any such

109   alteration.

110   **2. Zaonega Formation and the FAR DEEP core material**

111   FAR-DEEP drillholes 12A, 12B and 13A targeted the Zaonega Formation in the Onega

112   Basin of central Karelia, northwestern Russia (Fig. 1). Drilllholes 12A and 12B were drilled at

113   the same site, few metres apart (latitude 62.4947 N, longitude 35.2887 E). The reason for the two

114   holes from the same site is that drillhole 12A had to be aborted at the depth of ca. 100 m due to

115   technical problems. Drillhole 12B was drilled without sampling the core for the top 95 m and the

116   correlation between 12A and 12B was made using the lower contact of a large igneous body with

117   the underlying sedimentary rocks occurring at 95.45 m in 12A and 94.56 m in 12B. As these two

118   drillholes provide a continuous rock record, we refer to an integrated drillhole 12AB throughout

119   this article. Drillhole 13A is located approximately 25 km WNW of drillhole 12AB (latitude

120   62.5891 N, longitude 34.9273 E; Fig. 1). During the Paleoproterozoic, the investigated area was

121 part of the rifted flank of the Karelian craton and formed its continental margin to the

122 Svecofennian Ocean (Lahtinen et al., 2008; Melezhik et al, 1999).

123   The Zaonega Formation is a ca. 1500 m thick succession and consists of interbedded

124 sandstones, siltstones, basalts, limestones, dolostones, cherts, and mafic tuffs all of which are

125 intruded by gabbroic sills (Črne et al., 2013a,b; Galdobina, 1987). It occurs above the 400- to

126 800-m-thick Tulomozero Formation, a shallow marine-sabkha succession dominated by

127 carbonate rocks that preserve the Lomagundi-Jatuli isotopic signature (Brasier et al., 2011;

128 Melezhik et al., 2000). The nature of the contact between these two formations is unresolved and

129 interpretations vary from it being either conformable, or an erosional unconformity (Melezhik et

130 al., 2013), or a tectonic contact (Galdobina, 1987). A minimum age for the Zaonega Formation

131 of ca. 1.98 Ga is constrained by several whole-rock and mineral Sm-Nd and Pb-Pb isochrons on

132 a mafic-ultramafic sill of the overlying Suisari Formation (Puchtel et al., 1998; 1999), which is

133 consistent with a Re-Os age of ca. 2.05 Ga obtained on organic matter from the Zaonega

134 Formation (Hannah et al., 2008). The depositional age of the underlying Tulomozero Formation

135 has been constrained by a Pb-Pb age on dolomite of 2.09±0.07 Ga (Ovchinnikova et al. 2007).

136 Termination of the Lomagundi-Jatuli isotope excursion occurred at 2.06 Ga in Finland and Kola,

137 Russia (Karhu, 1993; Martin et al., 2013; Melezhik et al., 2007), but no definite ages exist for the

138 Karelian succession. Thus the maximum-minimum constraints of 2.09±0.07 and 1.98 Ga for the

139 Zaonega Formation indicate its deposition partly overlapped with and/or post-dated the

140 Lomagundi-Jatuli Event.

141   The presence of lavas and gabbroic sills, some with peperite contacts, throughout the

142 entire Zaonega Formation indicates a tectonically and magmatically active depositional setting.

143 Thick intervals of massive organic-rich rocks, commonly associated with mafic lava flows and

144 gabbroic sills, have been interpreted to result from hydrocarbon generation and migration either

145 within the already deposited succession in the form of diapirs (Filippov, 1994) or as

146 hydrocarbon-rich/asphalt spills on the sea-floor (Melezhik et al., 2004; Qu et al., 2012; Strauss et

147 al., 2013). Cavities associated with migrated hydrocarbons provide evidence for generation of

148 fluids , possibly in the form of SO_2, CO_2, and/or CH_4 (Qu et al., 2012; Strauss et al., 2013).

149   The succession recovered by the FAR-DEEP cores 12AB and 13A (Fig. 2) was divided

150 into four lithostratigraphic units, from bottom to top, the Greywacke, Dolostone-Greywacke,

151 Mudstone-Limestone, and Dolostone-Chert members (Črne et al., 2013a,b). The major facies

152   change at the boundary between the Mudstone-Limestone and Dolostone-Chert members

153   occurring at 9.3 m in core 12AB and at 76.6 m in core 13A is used for correlating the cores (Črne

154   et al., 2013b). The cored rock represent a deep-water, mixed siliciclastic-carbonate depositional

155   system with voluminous mafic volcanism and turbidity-current deposits represented by flat-

156   laminated, normally graded greywackes interbedded with mudstones, dolostones and limestones;

157   rare debrites are the result of erosion and redeposition within the basin, whereas thick mudstone

158   packages represent background hemipelagic sedimentation (Črne et al., 2013a). Several

159   consecutive intervals of massive organic-rich rocks sandwiched conformably by laminated

160   mudstones (Črne et al, 2013a; 156-133 m in drillcore 12AB; Fig. 2) are interpreted as

161   hydrocarbon-rich/asphalt spills on the sea-floor (Qu et al., 2012; Strauss et al., 2013).

162   Carbonate beds are present throughout the stratigraphy and their abundance, thickness

163   and textural characteristics are distinctive to each lithostratigraphic member. The Greywacke

164   member contains individual, thin beds of sandy limestone that thicken to several decimeters

165   towards the top of the member, where carbonate concretions were recognized (Črne et al.,

166   2013a). Because it is difficult to identify diagenetic carbonate concretions and layers as such if

167   they have lateral dimensions greater than the width of the core, it is possible that they occur in

168   places in the stratigraphy. The depositional mechanism considered to be most likely for the

169   Zaonega primary carbonates, is the shedding of carbonate from the shallow-water environment

170   into the deeper basin. This is supported by a carbonate bed within the Greywacke member,

171   which contains re-crystallized ooids indicating re-deposition of allochems within the

172   Paleoproterozoic Onega Basin. Above this, dolostones and sandy dolostones of the Dolostone-

173   Greywacke member occur as several-metres-thick, flat-laminated layers, or as metre-thick,

174   massive beds. The carbonate beds of the Mudstone-Limestone member are thinner, a few

175   decimetres-thick and indistinctly laminated or massive. The uppermost part of the stratigraphy is

176   typified by thick-bedded massive dolostone. We chose from one to three carbonate beds from

177   each of the members thereby spanning most of the cored Zaonega Formation (Fig. 2).

178

179   **3. Sampling and methods**

180   A total of 39 bulk and 29, 1-2 mm diamond-drilled samples were obtained from eight

181   carbonate beds and analyzed at the Geological Survey of Norway (NGU),the Scottish

182   Universities Environmental Research Centre (SUERC), East Kilbride, Scotland, and at the

183 University of Munster in Germany (Fig. 3; Table A1 in Appendix A). Major and trace elements

184 were analyzed at NGU by X-ray fluorescence spectrometry using a PANalytical Axios at 4 kW

185 and elemental concentrations were determined on acidified extracts (cold 10% HCl acid) by

186 inductively coupled plasma-atomic emission spectrometry (ICP-AES) using a Thermo Jarell Ash

187 ICP 61. Total sulphur (TS), total organic carbon (TOC), and total carbon (TC) were determined

188 at NGU (16 samples) and at University of Munster (23 samples). At NGU sealed tube

189 combustion using a Leco SC-444 had a total analytical uncertainty of 15%. For measurements of

190 TOC, the samples were reacted with 10% HCl acid before the combustion and inorganic carbon

191 (IC) was calculated from TOC and TC. At University of Munster the IC was determined by

192 reactions with 2 N perchloric acid ($HClO_4$) and TC by combustion of the sample; TOC was

193 calculated from TC and IC. The 29 drilled samples and 39 bulk samples were analyzed for stable

194 carbon and oxygen isotopes at SUERC using conventional procedures. For analyses of stable

195 carbon and oxygen isotopes approximately 1 mg of sample was reacted overnight with

196 phosphoric acid at 70ºC and stable carbon and oxygen isotopes ratios were measured on the

197 purified CO_2 using a SIRA II mass spectrometer. Twenty samples were analyzed for stable

198 carbon and oxygen isotope ratios by sequential extraction of CO_2 in two steps. The first step

199 included reaction of several tens of milligrams of sample with phosphoric acid for three hours in

200 a water-bath at 25ºC. As a second step, the remaining sample was reacted with phosphoric acid

201 overnight in a hot-block at 100ºC. The amount of CO_2 was measured after each step and the

202 carbon and oxygen isotopic composition was measured using a SIRA II mass spectrometer; the

203 precision and accuracy are difficult to specify since they will depend on the efficacy of the

204 sequential extraction procedure and the absolute and relative amounts of different carbonate

205 phases present, but ±0.5 ‰ seems a conservative working estimate (Table A2 in Appendix A).

206 Carbon and oxygen isotopic values are reported and discussed in the conventional delta notation

207 relative to Vienna Pee Dee Belemnite (VPDB).

208 Petrographic characterization of 19 polished thick sections (ca. 200µm in thickness), at

209 least two from each carbonate bed, involved backscattered electron imaging with a scanning

210 electron microscope (SEM-BSE) and the use of cathodoluminescence (CL). SEM-BSE work was

211 done at NGU using an SEM Leo1450VP in low vacuum mode at 16 Pa, an acceleration voltage

212 of 15 kV and a beam of 80 µA. The CL work was done at Karst Research Institute at Postojna,

213 Slovenia, using a CL8200 Mk4 instrument operating at 15 kV beam energy and a 400 mA beam.

214

3.1. Carbon and oxygen isotope analyses of carbonates by sequential extraction

Twenty samples from beds #1 to #7 were analyzed for carbon and oxygen isotopes by sequential extraction of CO_2 in two steps. $\delta^{13}C$ and $\delta^{18}O$ values were measured for each step of the reaction, after 3 hours at 25ºC and after an overnight reaction at 100ºC, and marked as $\delta^{13}C_1$, $\delta^{18}O_1$ for the first and $\delta^{13}C_2$, $\delta^{18}O_2$ for the second step. Due to differences in reaction rates of calcite and dolomite (Al-Aasm et al., 1990), we expected the $\delta^{13}C_1$, $\delta^{18}O_1$ and $\delta^{13}C_2$, $\delta^{18}O_2$ to correspond to the isotopic composition of calcite and dolomite, respectively. In order to evaluate whether the data from the two steps can be reasonably considered to correspond to calcite and dolomite, we compared the amounts of calcite and dolomite determined by ICP-AES for each sample with the measured amount of CO_2 extracted after each step.

The majority of the calcite-dominated (Mg/Ca<0.1) and dolomite-dominated (Mg/Ca>0.5) samples of the Zaonega Formation show relatively small, up to 2.5 ‰ differences of $\delta^{13}C$ between the two steps of extraction (Fig. 4; Table A2). Exceptions are the calcite-dominated sample in bed #6 (difference in $\delta^{13}C$ between the two steps is 5 ‰) and two dolomite-dominated samples from the bed #1 (difference in $\delta^{13}C$ between the two steps is 4 ‰). The relatively large differences in $\delta^{13}C$ between the two steps within the samples, where geochemical data suggest a single carbonate phase of either calcite or dolomite, might be due to the extraction-related kinetic isotopic effect but more likely to isotopic heterogeneity of the sample. During dissolution of dolomite-dominated samples, when a small amount of sample reacts during the first step, anomalously ^{13}C-depleted CO_2 could be produced due to an extraction-related kinetic effect, the result being a lower $\delta^{13}C_1$ value in comparison to the $\delta^{13}C_2$. For the calcite-dominated samples a large amount of sample dissolves after the first step (ca. 60 % of the whole sample reacts in 3 hours, Al-Aasm et al., 1990) and therefore the kinetic effect appears unlikely to be the reason for the differences between $\delta^{13}C$ of the two steps. Differences between $\delta^{13}C_1$ and $\delta^{13}C_2$ can also occur in either a dolomite- or calcite-dominated sample, if isotopic heterogeneities are coupled with differences in dissolution rates, e.g. an Fe-poor calcite/dolomite has a different isotopic composition than Fe-rich calcite/dolomite.

Based on our dataset and published reaction rates for calcite and dolomite at different temperatures (Al-Aasm et al., 1990), we conclude that the results of the two-step sequential extraction method may be used as an approximation of carbon and oxygen isotope signatures of

245 calcite and dolomite for those samples that contain significant relative amounts of each mineral

246 phase (>5 wt% of all carbonate). Predominance of either of the two mineral phases results in a

247 mixed signal in either of the two steps, complicating the determination of the isotopic differences

248 between calcite and dolomite. We have therefore interpreted the $\delta^{13}C_1$, $\delta^{18}O_1$ and $\delta^{13}C_2$, $\delta^{18}O_2$ to

249 represent calcite and dolomite respectively for the samples with the following characteristics: i)

250 general correspondence between amounts of calcite and dolomite determined by ICP-AES and

251 the measured amount of CO_2 extracted at each step; and ii) presence of a significant relative

252 amount of each mineral phase (>5 wt% of all carbonate). Other results of the sequential

253 extraction method on the Zaonega samples can be used for determination of isotopic

254 homogeneity of the samples and/or for assessment of the applicability of the method for the

255 Zaonega carbonates. Large differences in $\delta^{13}C$ between the two steps for the samples containing

256 either pure calcite or pure dolomite imply a limited applicability of the sequential extraction

257 method for all the samples of the Zaonega Formation such that an isotopic variability a few per

258 mil of needs to be taken into account.

259

260

261   **4. Results**

262 The aims of detailed sampling, geochemical analyses and petrographic characterization were: i)

263 assessment of $\delta^{13}C$ variability within single carbonate beds; and ii) determination of mineralogy

264 and textures of carbonate phases and associated minerals. Geochemical results include analyses

265 of 39 samples for stable carbon and oxygen isotopes, TOC/IC, ICP-AES, and XRF for eight

266 carbonate beds, together with the 29 additional closely spaced samples analyzed only for carbon

267 and oxygen isotopes. The textural characterization of carbonate minerals is based on SEM-BSE

268 and CL images of thin sections. Individual samples represent 12-cm-long quarters of the core

269 taken continuously along the whole thickness of carbonate beds, while one bed (#5) was sampled

270 from core to top. The positions of sample points in Figures 3 and 4 correspond to the tops of

271 individual 12-cm-long samples. The response of carbonate beds to 5 % HCl was monitored

272 during core logging: blue-colored lithologies in Figures 3 and 4 mark intensive reactions whereas

273 violet-coloring indicates lithologies that did not react to the acid (in Figs. 3 and 4).

274

275 *4.1. Geochemistry*

276   Selected geochemical parameters plotted along eight carbonate beds are presented in
277   Figure 3, and results from the carbon and oxygen analyses by sequential extraction are shown in
278   Figure 4. Beds #1 to #6 are described together because they show similar within-bed $\delta^{13}C$
279   variability of several per mil, with middle portions having relatively higher $\delta^{13}C$ values
280   compared to the margins (exception is bed #3). Beds #7 and #8 have low within-bed variation of
281    $\delta^{13}C$ (≈2 ‰), hence their geochemical characteristics are described separately.
282
283   Beds #1 to #6
284   The $\delta^{13}C$ variability within these six, single beds ranges from 4 ‰ (bed #3) to 17 ‰ (bed
285   #6; Fig. 3). All beds, except #3, display a decline in $\delta^{13}C$ values from their central parts (from -9
286   to +8 ‰; Table 1) outward to their margins (from -19 to -4 ‰; Table 1). For bed #3, the lowest
287    $\delta^{13}C$ values occur at the base (-8 ‰) and increase consistently upward through the middle (-5 to -
288   6 ‰) and to the top (-4 ‰). $\delta^{18}O$ values only show minor variation throughout the beds, with
289   beds #1 and #6 having $\delta^{18}O$ a few per mil higher in their middle parts relative to their margins.
290   Middle parts of all beds contain higher wt% of carbonate (IC=10–11 wt%), and therefore lower
291   wt% of siliciclastic material in comparison to the bed margins. The main carbonate mineral in
292   the central part of the beds is dolomite, which is Fe-Mn-rich in beds #2 to #5 but Fe-Mn poor in
293   beds #1 and #6 (Fig. 3). Calcite prevails at the margins of all beds (exception is lower margin of
294   bed #1), coinciding with relatively low IC and $\delta^{13}C$ in comparison to the centres of the beds.
295   Calcite contains higher amounts of Sr, up to 320 ppm, in comparison to dolomite with Sr content
296   below 100 ppm; an exception is dolomite in bed #3 with Sr values up to 160 ppm.
297   Whole-rock content of Ca is mostly stable throughout bed thickness, the exception being
298   the upper margins of beds #3 and #6, which are considerably lower in Ca abundance. Mg whole-
299   rock content decreases either significantly (beds #3, #4, #5, #6) or slightly towards the bed
300   margins (beds #1 and #2), broadly matching the trend of IC and $\delta^{13}C$ (exceptions are margins of
301   beds #1 and #3). The majority of beds with Fe-Mn-rich dolomite in the centres, (beds #2 and #5),
302   contain Fe-Mn-rich calcite at the bed-margins; Fe-poor, Mn-rich calcite is present at the margin
303   of bed #4 and Fe-Mn-poor calcite at the margin of bed #3. Beds #1 and #6, having Fe-Mn-poor
304   dolomite in their centre, also contain Fe-Mn-poor calcite at their margins.
305
306   Beds #7 and #8

307   The main characteristic of these two beds is that there are no significant differences in
308   geochemical compositions from their centres to margins (Fig. 3). The δ^{13}C variability is 2 ‰ in
309   bed #7 and 0.3 ‰ in bed #8. The δ^{18}O values are stable in both beds (ca. -17 ‰ in bed #7 and -
310   18.5 ‰ in bed #8). Amounts of carbonate and siliciclastic material are stable in bed #8 and
311   inversely proportional in bed #7, ranging from 7 to 10.4 wt% IC and from 7 to 21 wt% SiO_2. The
312   main carbonate phase in both beds is calcite with Sr content below 110 ppm, which is
313   significantly lower than the Sr content of calcite in beds #1 to #6. Whole-rock content of Mg is
314   low, only a few wt%.
315
316   *4.2. Textural properties of carbonate minerals*
317   Petrographic studies were performed to identify the carbonate components, characterize
318   their microtextures and interrelationships, and assess genetic associations with other mineral
319   phases. At least two thin sections were studied from each of the eight beds, one from the centre
320   of the bed and the other close to the margin of the bed. Samples were characterized by SEM-BSE
321   (hereafter BSE) imaging and cathodoluminescence (Figs. 5, 6 and 7). The beds with common
322   textural properties are described together: i) beds #2 to #5 contain zoned Fe-Mn-rich dolomite;
323   ii) beds #1 and #6 contain homogenous Fe-Mn-poor dolomites; iii) beds #7 and #8 contain low-
324   Sr calcite.
325
326   Beds #2 to #5
327   The middle parts of these beds contain zoned dolomite crystals ca. 20 μm in size, either
328   in tightly intergrown indistinct rhombohedric shapes and zones (beds #2 to #4; Figs. 5a, 5d and
329   5g) or rather loosely packed but well-defined rhombohedra with distinct zones; the latter is
330   cemented by dolomite (bed #5; Fig. 5j). Using CL, dolomite is nonluminescent in all samples
331   (e.g. Fig. 5f), only in bed #5 do rhombohedric rims and very few cores show bright red
332   luminescence (Fig. 5l). A significant amount of calcite, in places intergrown with quartz (bed #3;
333   Fig. 5d) and overgrowing dolomite or infilling spaces in partially dissolved dolomite, is present
334   in the middle parts of beds #2 to #4; these beds also contain abundant mica (mostly phlogopite;
335   talc is present in bed #2) and pyrite formed at different stages of diagenesis/metamorphism (Figs.
336   5b and 5d).

337   The margins of these beds contain mostly calcite occurring as smaller (beds #2 and #4) or
338   larger (bed #3), irregularly shaped patches usually intergrown with either quartz (bed #2 and #3;
339   Figs. 5b and 5e) or albite (bed #4; Fig. 5h). Albite occurs also as larger grains/patches, which
340   could be of detrital origin or a product of albitization of older grains, for example plagioclase or
341   sulfide. Dolomite is only present in the margin of bed #5 which contains mostly Ca and Fe-rich
342   dolomite as cement around the dolomitic rhombohedra and some calcite (Fig. 5k). Under CL,
343   calcite luminesces orange with a moderate to bright intensity (e.g. Figs. 5c and 5i). Micas in beds
344   #3 to #5 and talc in bed #2 are more abundant near bed margins than in the centre of the beds.
345
346   Beds #1 and #6
347   The middle parts of these two beds show large, tightly intergrown dolomite crystals ca.
348   70 μm in size (Figs. 6a and 6e); in bed #6, the crystals are so tightly packed that their shapes are
349   difficult to recognize, and only in places are rhombohedra observed. Dolomite crystals are
350   mostly homogeneous in BSE imagery with slightly darker cores in comparison to the outermost
351   parts (the transition is gradual). The contacts between crystals are straight to sutured (Fig. 6e).
352   Under CL most dolomite crystals show very dull red luminescence, some have dull luminescent
353   cores and bright rims, and in bed #1 a few crystals show bright-dull-bright zoning (Fig. 6c).
354   Calcite, mica and talc are present, but in minor amounts in comparison to the margins of the
355   same beds.
356   The lower margin of bed #1 mostly contains dolomite, whereas calcite is the dominant
357   carbonate mineral at the margin of bed #6. The former displays large dolomite crystals ca. 70 μm
358   in size and mostly tightly intergrown with recognizable rhombohedral shapes (Fig. 6b). Inner
359   parts of the crystals are brighter in BSE images in comparison to their outer parts (Fig. 6b).
360   Under CL, dolomite crystals are mostly zoned (dull-bright-dull luminescence), but many are dull
361   with bright rims (Fig. 6d). Where dolomite crystals are less tightly packed, micas and organic
362   matter occur in the interstices. Minor amounts of calcite are present. The margin of bed #6
363   contains calcite intergrown with quartz (dolomite is not observed, Fig. 6f). Talc and phlogopite
364   are more abundant at the margin than at the centre of the bed.
365
366   Beds #7 and #8

367   Bed #8 contains large (ca. 100 μm in size) patches of irregularly shaped calcite with

368   numerous embayments, tightly intergrown with albite (Fig. 7d). The middle part of bed #7

369   contains ca. 20 μm-large BSE homogeneous calcite crystals with albite intercalations; boundaries

370   between the crystals are straight and undulate (Fig. 7a). Albite, micas (phlogopite, chlorite) and

371   titanite are present in both beds, with albite occurring as spherical inclusions within calcite and

372   as rectangular grains in bed #7 (Fig. 7a) and as a mineral phase intergrown with calcite in bed #8

373   (Fig. 7d). Micas overgrowing calcite are more abundant in bed #8. Disseminated titanite is

374   present in both beds. Actinolite is only present in bed #8, overgrowing all mineral phases. Under

375   CL, calcite in both beds has medium-dull red luminescence, but a few small areas are bright red

376   (Fig. 7c).

377   The upper margin of bed #7 contains up to 0.5 mm large rhombohedra having a calcitic

378   core and an outer rim of calcite (Fig. 7b). The calcite forming the core is homogenous in BSE

379   images and contains spherical inclusions of albite of a few μm in size (Fig. 7b). The calcitic rim

380   contains spherical inclusions of quartz a few μm in size. Numerous inclusions of quartz mark the

381   sharp, but undulated boundaries between the core and rim (Fig. 7b). The outer boundary of the

382   calcitic rim to the surrounding quartz matrix is irregular with numerous embayments. Titanite

383   occurs predominantly together with micas in the quartz matrix, but also in the calcite rims and in

384   the cores of the rhombohedra. Micas overgrow all mineral phases.

385

386   **5.   Discussion**

387   *5.1. Primary and secondary carbonate precipitates – textural and geochemical indications*

388   On the basis of geochemical data, four main carbonate phases have been identified: i) Fe-

389   Mn-poor dolomite (bed #1 and centre of bed #6) and; ii) Fe-Mn-rich dolomite (centres of beds #2

390   to #5); iii) calcite, relatively rich in Sr (hereafter Sr-rich calcite; margins of beds #1 to #6); and

391   iv) calcite relatively poor in Sr (hereafter Sr-poor calcite; beds #7 and #8). Geochemical and

392   textural properties of these four carbonate phases, relevant to their relative order of formation,

393   are discussed below (overview of textural properties is shown in Figs. 8a-n).

394   The Fe-Mn-poor dolomite consists mostly of ≈70 μm-large homogenous crystals, which

395   are very tightly intergrown and have a dull red luminescence under CL; only a few crystals

396   (middle part of bed #1) have clearly distinguishable dull red cores and bright red rims under CL

397   (Fig. 6c). Homogenous textures of the Fe-Mn-poor dolomite crystals imply stable conditions

398   during their precipitation in the sedimentary/early diagenetic environment and/or during burial

399   recrystallization. Tight crystal intergrowth, likely developed during burial, could have prevented

400   intensive infiltration of later fluids. The Fe-Mn-poor dolomite is overgrown by texturally later

401   Sr-rich calcite.

402   The Fe-Mn-rich dolomite consists of ≈20 μm large, zoned rhombohedric crystals, which

403   are mostly nonluminescent under CL; only a few crystals (bed #5) show bright red luminescent

404   rims and very few of them possess also luminescent cores. Nonluminescence under CL is

405   presumed to be due to quenching by iron in these cases (Machel, 2000). Zoned crystals indicate

406   variable geochemical conditions during precipitation, either due to a closed system as the pore

407   waters are progressively depleted in certain species, or due to infiltration of fluids with a

408   different geochemical signature. The Fe-Mn-rich dolomite is overgrown by the Sr-rich calcite,

409   indicating relatively early formation of Fe-Mn-rich dolomite in relation to the calcite.

410   The Sr-rich calcite in beds #1 to #6 forms irregular patches containing either albite or

411   quartz inclusions and overgrows both types of dolomite in the centres of the beds; this calcite

412   thus formed relatively late with respect to dolomite. The amount of Sr-rich calcite varies along

413   the thickness of each bed, being least at the centres of the beds and greatest at the bed-margins:

414   at the margins of beds #2, #3, #4, and #6, we find only calcite. While the timing of calcite

415   precipitation is more difficult to verify at the bed margins because only one carbonate phase is

416   present, we interpret the calcite at the centres and at the margins of the same beds as an identical

417   phase due to textural similarities (Figs. 5-7). The δ^{13}C values of Sr-rich calcite in the studied

418   beds are between -19 ‰ and -4 ‰ (samples with Mg/Ca<0.1 in Fig. 8a), which is as much as 17

419   ‰ lower in comparison to the dolomite-dominated samples occurring within the same beds

420   (Figs. 3, 4, 8a). Significantly different carbon isotope composition, and relatively late formation

421   of Sr-rich calcite in comparison to dolomite implies different conditions for the dolomite and Sr-

422   rich calcite formation. This, together with the co-occurrence of calcite with secondary albite and

423   quartz, suggests that the Sr-rich calcite formed later in the post-depositional history of these

424   rocks than the dolomite.

425   The Sr-poor calcite does not occur in conjunction with any other carbonate phase, making

426   it difficult to assess its place in the paragenetic sequence. Texturally, however, the Sr-poor

427   calcite in beds #7 and #8 is comparable to the Sr-rich calcite on the outer margins of beds #1 to

428   #6; i.e. mostly irregularly shaped calcite patches inter-grown with either quartz or albite. Further,
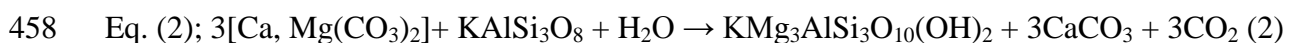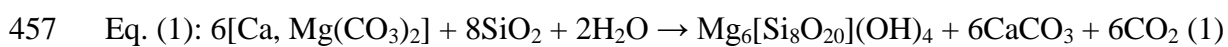
429   the Sr-poor calcite is associated with actinolite in bed #8, which is located 20 m above a 70-m-

430   thick mafic intrusion (Fig. 2). It is most probable that the Sr-rich and Sr-poor calcite formed

431   under similar conditions, the Sr-poor calcite probably at higher temperatures as indicated by the

432   presence of actinolite, implying precipitation of the Sr-poor calcite later than the dolomite.

433   Rhombohedral calcite patches in bed #7 (Fig. 7b) could have formed through complete

434   calcitization of dolomite rhombohedra. The large size of the former suggests their initial

435   formation, or recrystallization, during burial and a later formation of Sr-poor calcite. Small Sr-

436   poor calcite crystals in the centre of bed #7 have well preserved crystal boundaries and likely

437   represent the least altered sedimentary calcite. The $\delta^{13}C$ and $\delta^{18}O$ values of all Sr-poor calcite,

438   however, are low and fall within the range of the $\delta^{13}C$ and $\delta^{18}O$ values of the Sr-rich calcite (Fig.

439   8d), inferred to reflect post-depositional formation or alteration of earlier carbonates. It is

440   therefore most probable that the small calcite crystals in bed #7 are also of post-depositional

441   origin, or at least their carbon and oxygen isotopic composition have been reset. There may be

442   some primary calcite in bed #7, but the carbon isotope composition of this bed ($\delta^{13}C$ = -11 ‰)

443   and co-occurrence of calcite with albite or quartz is similar to the clearly post-depositional

444   calcite in other beds.

445   In summary, dolomites of both types likely represent primary or early diagenetic

446   carbonate precipitates within the Zaonega Formation, whereas calcite mostly formed as a

447   relatively late carbonate phase precipitating under variable post-depositional, including

448   hydrothermal conditions. This latter interpretation is based on the observation that, within the

449   same samples, calcite overgrows dolomite and has textural association with secondary quartz and

450   albite.

451

452   *5.2. Formation of secondary carbonates*

453   The calcite ± talc ± phlogopite ± actinolite paragenesis observed in carbonate beds indicates that

454   the following volatilization reactions could have been the pathway influencing $\delta^{13}C$ and $\delta^{18}O$

455   composition of residual dolomite and newly formed calcite (Bucher and Frey, 2002; Shieh and

456   Taylor, 1969):

457   Eq. (1): $6[Ca, Mg(CO_3)_2] + 8SiO_2 + 2H_2O \rightarrow Mg_6[Si_8O_{20}](OH)_4 + 6CaCO_3 + 6CO_2$ (1)

458   Eq. (2); $3[Ca, Mg(CO_3)_2] + KAlSi_3O_8 + H_2O \rightarrow KMg_3AlSi_3O_{10}(OH)_2 + 3CaCO_3 + 3CO_2$ (2)

459

460   The CO_2 produced by such reactions can be enriched in ^{13}C and [18]O in comparison to the original

461   dolomite due to equilibrium isotopic fractionation between CO_2 and dolomite (Shieh and Taylor,

462   1969; Valley, 1986), and in high-temperature greenschist metamorphic conditions the $\delta^{13}C$ of the

463   calcite produced was found to be up to 4 ‰ lower than the co-occurring dolomite (e.g. Melezhik

464   and Fallick, 2003; Melezhik et al., 2003). The mineralogy of carbonate beds #1 to #6 is

465   consistent with such alterations, containing reactants (dolomite, quartz) and all the products

466   (phlogopite, talc, and calcite). The reason for the lack of K-feldspar in carbonate beds could be

467   its initial absence, or could be due to complete reaction of K-feldspar with the co-occurring

468   dolomite. Mineral associations together with ^{13}C-depletion of calcite imply that Sr-rich calcite

469   formed as a metamorphic reaction product as described by the equations above. The magnitude

470   of $\delta^{13}C$ depletion of calcite relative to dolomite is as much as 17 ‰. This cannot be due to

471   volatilization alone and requires a ^{13}C-depleted fluid to explain the low $\delta^{13}C$ values of the calcite

472   (Valley, 1986). It is known that large changes in the carbon and oxygen isotope compositions of

473   carbonate rocks can be due to extensive fluid-rock interaction at low metamorphic temperatures

474   (e.g. Guerrera et al., 1997). As the deposition of the Zaonega rocks was accompanied by

475   contemporaneous vigorous magmatic activity, formation of peperites, oil generation and seeping

476   and spilling of hydrocarbons (Črne et al., 2013a,b; Melezhik et al., 2009; Qu et al., 2012), it is

477   reasonable to infer that intense hydrothermal fluid circulation supplied water, silica, CO_2 (likely

478   as carbonic acid) and CH_4 to the depositional system (Strauss et al., 2013).

479   There are abundant possible ^{13}C-depleted sources within the Zaonega Formation:

480   volcanic CO_2 with assumed $\delta^{13}C$ ca. -5 ‰, ample organic matter with $\delta^{13}C$ between -25 and -42

481   ‰ (Filippov and Golubev, 1994; Kump et al., 2011; Qu et al., 2012) and its catagenetic products

482   (including organic acids and biogenic methane), and inferred thermogenic methane (Qu et al.,

483   2012) with $\delta^{13}C$ likely between -20 and -50 ‰ (for precursor organic carbon at -25 ‰)

484   (Whiticar, 1999). Although volcanic CO_2 might have played an important role in hydrothermal

485   fluids, it does not in any clear way facilitate precipitation of calcite with $\delta^{13}C$ values lower than -

486   5 ‰. Oxidation of organic matter forming CO_2 or bicarbonate must have occurred in order to

487   explain the very low $\delta^{13}C$ values of the secondary calcite. No measured $\delta^{13}C$ of secondary

488   carbonate demands the involvement of oxidized CH_4, although we recognize that it is

489   geologically reasonable that both biogenic and thermogenic methane were available at various

490   times. Sedimentary rocks within the drilled succession are rich in TOC; mudstones, which are by

491   far the most abundant lithology encompassing the studied carbonate beds in FAR-DEEP cores

492   12AB and 13A, may contain more than 20 wt% of TOC (Črne et al, 2013a,b).

493   Decomposition of organic matter can be facilitated by thermochemical and bacterial

494   processes of sulfate, iron, or manganese reduction, all plausibly sourced from minerals within the

495   Tulomozero and Zaonega formations, and from seawater; H_2O itself is a likely source of oxygen

496   once the oil window is reached. The sulfur isotope data from the Zaonega (Shatsky, 1990) and

497   Pilgujarvi Formations (Melezhik et al., 1998), the latter a unit on the Kola Peninsula that is

498   broadly correlative to the Zaonega Formation (Hannah et al., 2006), indicate presence of sulfate

499   in contemporaneous sea-water enabling sulfate reduction during deposition (Reuschel et al.,

500   2012). Sulfate may have also been supplied from the underlying Tulomozero Formation

501   containing abundant calcitized sulfates (Brasier et al., 2011; Melezhik et al., 2005) and even

502   thick anhydrite beds (Morozov et al., 2010). As the formation of ^{13}C-depleted calcite occurred

503   relatively late in comparison to the earlier formed dolomite (that was probably of sedimentary

504   and/or early diagenetic origin), it is likely that low ^{13}C carbon was supplied from different depths

505   during burial of the Zaonega sediments (cf. Irwin et al., 1977), followed by metamorphic

506   reactions and possible hydrothermal alterations. Whatever the source of the oxidants and

507   whatever the processes of oxidation, the solid organic matter or fluid hydrocarbons of the

508   Zaonega Formation had ample opportunity to be oxidized and supply ^{13}C-depleted CO_2 to the

509   post-depositional fluids.

510   The isotopic uniformity of carbonate beds #7 and #8, located in proximity to thick mafic

511   bodies, is tentatively interpreted to be the result of homogenization of $\delta^{13}C$ and $\delta^{18}O$ due to

512   pervasive post-depositional fluid infiltration associated with those intrusions. A somewhat

513   similar isotopic effect was reported by Frauenstein et al. (2009) from dolostones in near contact

514   with the Bushveld intrusive complex. The absence of talc within beds #7 and #8 could reflect the

515   actions of pervasive CO_2-rich fluid flow and/or high temperatures (>450 °C) within the lower

516   part of the succession, hindering talc formation and preservation (e.g. Bucher and Frey, 2002).

517   Alternatively, bed #7 may represent either a sedimentary layer or an early diagenetically formed

518   concretion with an original calcitic mineralogy, though (as with all carbonates here) now likely

519   recrystallised.

520   We interpret the pervasive calcitization of the margins of carbonate beds #1 to #6 as

521   caused by: i) reactions between quartz-rich mudstone and dolomite in the presence of

522   hydrothermal fluids; and ii) potential early lithification of the carbonates relative to the organic-

523   rich mudstones resulting in differences in permeability between the two lithologies, thus

524   channeling fluid flow at lithological boundaries. A larger amount of secondary calcite at the bed

525   margins fits a hypothesis of flow of post-depositional fluids along lithological contacts. The

526   intensity of rock-fluid interaction can be approximated by differences in composition between

527   newly formed calcite and its presumed dolomite precursor, up until the point of total resetting. In

528   beds #3 and #4, the calcite is Fe-Mn-poor even though the dolomite within the same bed is Fe-

529   Mn-rich. This can be interpreted as due to greater fluid mobilization in this part of the

530   stratigraphy: both beds are located in close proximity to asphalt spills (Fig. 2; bed #3 is also

531   closer to the magmatic body). High amounts of Fe and Mn in dolomite and calcite in beds #2 and

532   #5 suggest a partly inherited geochemical signature of calcite from its dolomite- precursor and

533   therefore imply less intense fluid mobility and/or interaction in this part of the succession. Less

534   prone to secondary overprints were those carbonate beds that: i) contain tightly intergrown

535   dolomite crystals that inhibited pervasive fluid infiltration; and ii) have the highest initial

536   carbonate content, thereby buffering the carbon isotopic system to a larger degree (δ^{13}C is

537   correlative to IC, see Fig. 8c). Noteworthy, though, is that all studied samples show variable

538   signs of alteration as evidence that even the 'best' samples (in terms of preserving

539   original/primary carbonate geochemical signatures), contain secondary calcite (e.g. BSE image

540   of the sample from the centre of bed #6 shown in Fig. 6e).

541   Regional greenschist metamorphism at 1.8 Ga could have additionally altered the

542   geochemistry of the Zaonega carbonate rocks. The Zaonega Formation as a whole underwent

543   low- to middle-temperature greenschist-grade regional metamorphism with temperatures of 300

544   to 350$^\mathrm{o}$C (Volodichev, 1987); the presence of actinolite (bed #8) indicates locally higher

545   temperature conditions close to the mafic intrusions. Secondary actinolite and albite-calcite

546   intergrowth in proximity to contacts with peperites implies formation of these minerals in

547   relation to mafic intrusions and therefore prior to complete lithification. It is therefore likely that

548   some calcite formed locally as a secondary mineral of hydrothermal/metasomatic origin before

549   the regional metamorphic event, while some might have formed earlier, perhaps during early

550   (syn-sedimentary?) diagenesis (e.g. bed #7), and we do not entirely exclude a possible initial

551   calcitic mineralogy of some carbonate beds.

552   In summary, the lower part of the Zaonega succession might have experienced extensive
553   fluid circulation causing complete calcitization of carbonate beds, although their original calcite
554   mineralogy cannot be excluded. In the upper part of the succession calcitization was restricted to
555   bed-margins. Samples in centres of beds, containing largely dolomite and little calcite, are most
556   easily interpreted as belonging to the least-altered carbonate samples of the Zaonega Formation,
557   and as the most likely to have preserved the δ^{13}C signal of ambient sea-water.

558
559   *5.3. Preliminary implications for the Zaonega δ^{13}C record and global Paleoproterozoic events*
560   Our results show that all studied carbonate samples have been to varying degrees affected
561   by post-depositional alteration. The least altered carbonate samples are in the centres of
562   carbonate beds composed mainly of dolomite in a tightly intergrown crystal texture and
563   containing little calcite. One current approach to identify the best-preserved carbonates within
564   the Zaonega Formation is identifying those with the highest amount of dolomite, as these are the
565   samples with the highest carbon isotope buffering capacity against secondary and subsequent
566   alterations. We have therefore used (Mg/Ca)*IC (Mg/Ca ratio multiplied by inorganic carbon) as
567   an approximation of the amount of dolomite to identify the best-preserved samples from this
568   study and those in the study of Kump et al. (2011) on the same drill core (Fig. 8b). Using our
569   (Mg/Ca)*IC metric, samples were categorized into four groups of assessed apparent alteration:
570   minor/moderate, significant, extensive, and complete (arbitrary boundaries at (Mg/Ca)*IC = 6;
571   3.5; 1; see Fig. 8b). Altogether 7 samples were found to belong to minor/moderately altered
572   caltegory: 5 samples from the set of 39 samples of this study and 2 samples from the dataset of
573   Kump et al. (2011). We acknowledge that such a discriminatory classification is inherently
574   biased against the possibility that a few of the calcites could have well-preserved carbon isotope
575   signatures, but our aim here is solely to ascertain the samples we can be most confident about.
576   Post-depositional alteration of the Zaonega carbonate rocks is also likely indicated by
577   cross-plots of δ^{13}C and δ^{18}O, as decreasing δ^{18}O values correspond to lower δ^{13}C values within
578   single beds (beds #1 and #6 in Fig. 8d). The non-primary calcites show a trend of decreasing
579   δ^{18}O values with depth, whereas the dolomites have δ^{18}O values slightly above the calcite δ^{18}O
580   values (Fig. 9). Well-defined stratigraphic trend of δ^{18}O implies that the oxygen isotope
581   composition of calcite represents complete homogenization or formation during post-
582   depositional alteration and that the alteration is successively stronger down the stratigraphy (Fig.

583   9). Oxygen isotope compositions can show complete homogenization as per those beds with

584   relatively low $\delta^{18}O$ values overlapping with those of non-primary calcite (beds #2 to #5, #7, #8

585   in Fig. 8d), or they can show less modification including distinctly higher $\delta^{18}O$ values than the

586   calcite, as per beds #1 and #6 (Fig. 8d). We have therefore used values of $\delta^{18}O$ for additional

587   screening of those samples, that were found to be minor to moderately altered on the basis of

588   (Mg/Ca)*IC metric. Minor to moderately altered samples were further subdivided such that those

589   with the highest $\delta^{18}O$ were interpreted to be least altered and most likely to be archiving $\delta^{13}C$

590   values closest to the initial composition (Fig. 8d). Two out of eight studied beds contain minor to

591   moderately altered samples: the line perpendicular to the $\delta^{13}C$ vs. $\delta^{18}O$ alteration trend defines

592   the least altered sample within each carbonate bed. Both minor to moderately altered samples

593   from the data-set of Kump et al. (2011) on the basis of (Mg/Ca)*IC metric are here considered as

594   least altered carbonate samples.We have linked all the samples to the Zaonega stratigraphy (Fig.

595   9) and these show a negative $\delta^{13}C$ shift with amplitude larger than 20 ‰ (Fig. 9). Comparing

596   screened to unscreened samples shows that the difference in values between the least- to most-

597   altered is larger than 10 ‰ within the same bed or within a 20–m-thick stratigraphic interval.

598   Hence, using our selective criteria, the amplitude of the $\delta^{13}C$ shift based on un-screened samples

599   cannot be straightforwardly interpreted as a result of changes in the global carbon cycle.

600   Examining all data, those in this study and those reported by Kump et al. (2011), only

601   four carbonate samples from two stratigraphic intervals can be considered convincingly in the

602   category least altered. These samples have $\delta^{13}C$ values of +8 ‰ and +4 ‰ in the middle part of

603   the section (at 250 m and 239 m in core 12AB), and -4 ‰ and -2 ‰ at the top (at 2 m in 12AB

604   and at 58 m in 13A, respectively; Fig. 9). Thus, using our admittedly strict screening criteria,

605   least-altered $\delta^{13}C$ values define a stratigraphic profile that is considerably different from the one

606   reported previously by Kump et al. (2011) (Fig. 9). If the least altered carbonates formed in

607   equilibrium with the $\delta^{13}C$ of the global CO_2, we can make the following conclusions about the

608    $\delta^{13}C$ of marine and atmospheric carbon at the time of deposition of the Zaonega sediments: i): i)

609   stratigraphically lowermost least-altered samples (250 and 239 m in core 12AB) have $\delta^{13}C$

610   values of +8 and +4 ‰, which are higher from that of the present; ii) among so far studied

611   carbonate samples, none is in the least-altered category in the stratigraphic interval between 239

612   m and 2 m in drillcore 12AB; conclusions about the changes in the global carbon cycle during

613   the time of deposition of this stratigraphic interval are currently not possible; and iii) the top of

614   the section is typified by $\delta^{13}C$ values of -4 ‰ and -2 ‰, which are lower from that at the present.

615   (Fig. 9).

616   Environmental conditions specific to the Paleoproterozoic Onega Basin, such as ample

617   organic matter, petroleum generation and seepage (Melezhik et al., 1999; 2009; Qu et al., 2012;

618   Strauss et al., 2013) could have influenced and lowered the $\delta^{13}C$ of the local dissolved inorganic

619   carbon pool. If the primary carbonates formed in such restricted conditions, they could reflect

620   more of a basinal than global $\delta^{13}C$ signal, whereas the non-primary carbonates should provide a

621   proxy to $\delta^{13}C$ of burial and metamorphic fluids. However, the inferred restricted basinal

622   conditions should not directly affect the isotopic composition of carbonate shedded to the

623   Zaonega basin from the shallow-water environment, which we infer as the main mechanism of

624   primary carbonate deposition based on sedimentological evidence. Much of the Zaonega

625   stratigraphy shows signs of post-depositional alteration and few least-altered samples were

626   convincingly recognized. This suggests that some primary carbonate supplied from the

627   environmentally decoupled shallower settings site might have experienced post-depositional

628   alteration in organic-rich environments in their final depositional location. We should therefore

629   apply caution when using non-discriminated $\delta^{13}C$ data of the Zaonega carbonate rocks to infer

630   functioning of the Paleoproterozoic global carbon cycle. Given these caveats, further detailed

631   sedimentological and geochemical investigations of the Zaonega rocks, as well as carbonates and

632   organic matter of other sedimentary units of similar age elsewhere, are required to corroborate

633   the existence of a major perturbation of the global carbon cycle at this time (e.g. Kump et al.

634   2011).

635

636   **6. Conclusions**

637   Based on detailed textural and geochemical characterization of representative samples from the

638   carbonate rocks of the Paleoproterozoic Zaonega Formation, Karelia, Russia,we conclude:

639   i)   Dolomite is the early, most primary carbonate phase preserved within the

640   Zaonega Formation whereas the majority of the calcite formed during progressive

641   burial accompanied by possible hydrothermal alteration and metamorphic

642   carbonate-silicate reactions.

643   ii)   While many studied carbonate samples have been affected by post-depositional

644   alteration, the samples most easily interpreted as least-altered contain high

645   amounts of dolomite represented by tightly-intergrown crystals, and are located in

646   the central parts of thicker carbonate beds. These yield values of $\delta^{13}C$ of 8 ‰ in

647   the middle part of the succession and decline to -4 ‰ in the topmost part.

648   iii)   Extensive fluid circulation has permeated through the Zaonega succession causing

649   secondary calcitization of carbonate bed-margins and apparent complete

650   calcitization of some thin carbonate beds in the lowermost parts of the

651   stratigraphy close to the gabbro sill.

652   iv)   Calcite-talc±phlogopite±actinolite mineral paragenesis suggests calcitization

653   occurring through reactions of dolomite with quartz, or possibly K-feldspar, in the

654   presence of fluids. The possibility of an initial calcitic mineralogy of carbonates

655   that might represent sedimentary layers and concretions needs further assessment.

656   v)   When calcite and dolomite occur within the same carbonate bed, and the former is

657   significantly depleted in ^{13}C in comparison to the dolomite, this suggests the

658   formation of calcite due to infiltration of ^{13}C-depleted fluid probably sourced

659   from volcanic CO_2 and oxidation of organic matter.

660   vi)   In most intervals, the $\delta^{13}C$ signal of the primary carbonate lithologies has been

661   variably modified such that previously published carbon isotopic profiles of the

662   Zaonega Formation based on whole rock analyses should be viewed cautiously

663   with respect to their utility in assessing the Paleoproterozoic carbon cycle.

664   vii)   The apparent scarcity of least-altered carbonate rocks highlights the need for

665   additional study of all such units used to track the Paleoproterozoic carbon cycle

666   during the Paleoproterozoic oxidation of the Earth and the importance of careful

667   assessment for post-depositional alteration on the basis of geochemical and

668   petrographic properties.

669

677   **Appendix A. Supplementary data**

678   Supplementary data, Table A1 and A2, can be found at…

679

7. References

Al-Aasm, I.S., Taylor, B.E., South, B., 1990. Stable isotope analysis of multiple carbonate samples using selective acid extraction. Chem. Geol. (Isot. Geosci. Sect.) 80, 119–125.

Bekker, A., Holland, H.D., Wang, P.-L., Rumble III, D., Stein, H.J., Hannah, J.L., Coetzee, L.L., Beukes, N.J., 2004. Dating the rise of atmospheric oxygen. Nature 427 (6970), 117–120.

Baker, A.J., Fallick, A.E., 1989. Evidence from Lewisian limestones for isotopically heavy carbon in two-thousand-million-year-old sea water. Nature 337 (6205), 352–354.

Brasier, A.T., Fallick, A.E. Prave, A.R., Melezhik, V.A., Lepland, A., FAR-DEEP Scientists, 2011. Coastal sabkha dolomites and calcitised sulphaes preserving the Lomagundi-Jatuli carbon isotope signal. Precambrian Research 189, 193–211. doi:10.1016/j.precamres.2011.05.011.

Bucher, K., Frey, M., 2002. Petrogenesis of metamorphic rocks, Springer-Verlag, Berlin, 341 pp.

Črne, A.E, Melezhik, V.A., Prave, A.R., Lepland, A., Romashkin, A.E., Rychanchik, D.V., Hanski, E.J., Luo, Zh.-Y., 2013a. 6.3.3 Zaonega Formation: FAR-DEEP Holes 12A and 12B, and neighbouring quarries. In: Melezhik, V.A., Prave, A.R., Fallick, A.E., Hanski, E., Lepland, A., Kump, L.R., Strauss, H. (Eds.), Reading the Archive of Earth's Oxygenation, vol. 2, Springer, pp. 946–1007.

Črne, A.E, Melezhik, V.A., Prave, A.R., Lepland, A., Hanski, E.J., Romashkin, A.E., Rychanchik, D.V., Luo, Zh.-Y., 2013b. 6.3.4 Zaonega Formation: FAR-DEEP Hole 13A. In: Melezhik, V.A., Prave, A.R., Fallick, A.E., Hanski, E., Lepland, A., Kump, L.R., Strauss, H. (Eds.), Reading the Archive of Earth's Oxygenation, vol. 2, Springer, pp. 1008–1046.

Farquhar, J., Bao, H., Thiemens, M., 2000. Atmospheric Influence of Earth's Earliest Sulfur Cycle. Science 289, 756–758.

Filippov, M.M. (Eds.), 1994. The organic matter of Karelian Shungite rocks (Genesis, evolution and the methods of study). Kola Science Centre, Petrozavodsk, 208 pp. (in Russian)

Filippov, M.M., Golubev, A.I., 1994. Carbon isotope composition of shungite rocks, In: Filippov, M.M. (Eds.), The Organic Matter of Karelian Shungite Rocks (Genesis, Evolution and the Methods of Study), Karelian Research Centre, Petrozavodsk, pp. 32–43. (in Russian)

Frauenstein, F., Veizer, J., Beukes, N. Van Niekerk, H.S., Coetzee, L.L., 2009. Transvaal Supergroup carbonates: Implications for Paleoproterozoic $\delta^{18}O$ and $\delta^{13}C$ records. Precambrian Research 175, 149–160.

Galdobina, L.P., 1987. The Ludikovi superhorizon. In: Sokolov, V.A. (Eds.), Geology of Karelia, Nauka (Science), Leningrad, pp. 59–67. (in Russian)

724   Guerrera, A., Peacock, S.M., Knauth, L.P., 1997. Large ^{18}O and ^{13}C depletions in greenschist
725   facies carbonate rocks, western Arizona. Geology 25, 943–946.
726
727   Hannah, J.L., Stein, H.J., Zimmermman, A., Yang, G., Markey, R.J., Melezhik, V.A., 2006.
728   Precise 2004 ± 9 Ma Re-Os age for Pechenga black shale: comparison of sulfides and organic
729   material. Geochemica et Cosmochimica Acta 70, A228.
730
731   Hannah, J. L., Stein, H. J., Zimmerman, A., Yang, G., Melezhik, V.A., Filippov, M.M., Turgeon,
732   S.C., Creaser, R.A., 2008. Re-Os geochronology of shungite: A 2.05 Ga fossil oil field in
733   Karelia. Geochimica et Cosmochimica Acta 72 (12, Supplement 1), A351.
734   Irwin, H., Curtis, C., Coleman, M., 1977. Isotopic evidence for source of diagenetic carbonates
735   formed during burial of organic-rich sediments. Nature 260, 209–213.
736
737   Karhu, J.A., 1993. Palaeoproterozoic evolution of the carbon isotope ratios of sedimentary
738   carbonates in the Fennoscandian Shield. Geological Survey of Finland Bulletin 371, 1–87.
739
740   Karhu, J.A., Holland, H.D., 1996. Carbon isotopes and the rise of atmospheric oxygen. Geology
741   24, 867–870.
742
743   Krupenik, V.A., Akhmedov, A.M., Sveshnikova, K.Y., 2011. Isotopic composition of carbon,
744   oxygen and sulphur in the Ludicovian and Jatulian rocks. In: Glushanin, L.V., Sharov, N.V.,
745   Shchiptsov, V.V. (Eds.), Palaeoproterozoic Onega Structure (Geology, Tectonics, Deep Structure
746   and Mineralogeny) Karelian Research Centre, Russian Academy of Sciences, Petrozavodsk, pp.
747   250–255. (in Russian)
748
749   Kump, L.R., Junium, C., Arthur, M.A., Brasier, A.T., Fallick, A.E., Melezhik, V.A., Lepland, A.,
750   Črne, A.E., Luo, G., 2011. Isotopic evidence for massive oxidation of organic matter following
751   the great oxidation event. Science 334 (6063), 1694–1696, doi: 10.1126/science.1213999.
752   Lahtinen, R., Garde, A.A., Melezhik, V.A., 2008. Paleoproterozoic evolution of Fennoscandia
753   and Greenland. Episodes 31 (1), 9p.
754
755   Machel, H.G., 2000. Application of cathodoluminescence to carbonate diagenesis. In: Pagel, M.,
756   Barbin, V., Blanc, P., Ohnenstetter, D. (Eds.), Cathodoluminescence in geosciences, New York,
757   Springer, pp. 271–301.
758
759   Martin, A.P., Condon, D.J., Prave, A.R., Melezhik, V.A., Lepland, A., Fallick, A.E., 2013.
760   Dating the termination of the Palaeoproterozoic Lomagundi-Jatuli carbon isotopic event in the
761   North Transfennoscandian Greenstone Belt. Precambrian Research 224, 160–168.
762
763   Melezhik,V.A., Fallick, A.E., 1996. A widespread positive $\delta^{13}C_{carb}$ anomaly at around 2.33-2.06
764   Ga on the Fennoscandian Shield: a paradox? Terra Nova 8, 141-157.
765
766   Melezhik, V.A., Fallick, A.E., 2003. $\delta^{13}C$ and $\delta^{18}O$ variations in primary and secondary
767   carbonate phases: several contrasting examples from Palaeoproterozoic C-13-rich
768   metamorphosed dolostones. Chemical geology 201 (3-4), 213–228.

769

770 Melezhik, V.A., Fallick, A.E., Filippov, M.M., Larsen, O., 1999. Karelian shungite - an
771 indication of 2.0-Ga-old metamorphosed oil-shale and generation of petroleum: geology,
772 lithology and geochemistry. Earth-Science Reviews 47, 1–40, doi: 10.1016/S0012-
773 8252(99)00027-6.

774

775 Melezhik, V.A., Fallick, A.E., Filippov, M.M., Lepland, A., Rychanchik, D.V., Deines, Y.E.,
776 Medvedev, P.V., Romashkin, A.E., Strauss, H., 2009. Petroleum surface oil seeps from a
777 Palaeoproterozoic petrified giant oilfield. Terra Nova 21, 119–126, doi: 10.1111/j.1365-
778 3121.2009.00864.x.

779

780 Melezhik, V.A., Fallick, A.E., Medvedev, P.V., Makarikhin, V.V., 2000. Palaeoproterozoic
781 magnesite–stromatolite–dolostone–'red bed' association, Russian Karelia: palaeoenvironmental
782 constraints on the 2.0 Ga positive carbon isotope shift. Norwegian Journal of Geology 80, 163–
783 186.

784
785 Melezhik, V.A., Fallick, A.E., Smirnov, Y.P., Yakovlev, Y.N., 2003. Fractionation of carbon and
786 oxygen isotopes in ^{13}C-rich Palaeoproterozoic dolostones in the transition from medium-grade to
787 high-grade greenschist facies: a case study from the Kola Superdeep Drillhole. Journal of the
788 Geological Society 160, 71–82.

789

790 Melezhik, V.A., Fallick, A.E., Rychanchik, D.V., Kuznetsov, A.B., 2005. Palaeoproterozoic
791 evaporates in Fennoscandia: implications for sea-water sulphate, the rise of atmospheric oxygen
792 and local amplification of the δ^{13}C excursion. Terra Nova 17, 141–148.

793

794 Melezhik V.A., Filippov, M.M., Romashkin, A.E., 2004. A giant Palaeoproterozoic deposit of
795 shungite in NW Russia: genesis and practical applications. Ore geology reviews 24, 135–154.

796

797 Melezhik, V.A., Grinenko, L.N., Fallick, A.E., 1998. 2000-Ma sulphide concretions from the

798 `Productive' Formation of the Pechenga Greenstone Belt, NW Russia: genetic history based on

799 morphological and isotopic evidence. Chemical Geology 148 (1-2), 61–94.

800
801 Melezhik, V.A., Huhma, H., Condon, D.J., Fallick, A.E., Whitehouse, M.J., 2007. Temporal
802 constraints on the Paleoproterozoic Lomagundi-Jatuli carbon isotopic event. Geology 35, 655–
803 658, doi: 10.1130/G23764a.1.

804
805 Melezhik, V.A., Prave, A.R., Lepland, A., Romashkin, A.E., Rychanchik, D.V., Hanski, E.J.,
806 2013. 6.3.2 Tulomozero Formation: FAR-DEEP Hole 11A. In: Melezhik, V.A., Prave, A.R.,
807 Fallick, A.E., Hanski, E., Lepland, A., Kump, L.R., Strauss, H. (Eds.), Reading the Archive of
808 Earth's Oxygenation, vol. 2, Springer, pp. 889–945.

809
810 Morozov, A.F., Hakhaev, B.N., Petrov, O.V., Gorbachev, V.I., Tarkhanov, G.B., Tsvetkov, L.D.,
811 Erinchek, Y.M., Akhmedov, A.M., Krupenik, V.A., Sveshnikova, K.Y., 2010. Rock-salts in
812 Palaeoproterozoic strata of the Onega depression of Karelia (based on data from the Onega
813 parametric drillhole). Transection of Academy of Sciences 435 (2), 230–233. (in Russian)
814

815   Ovchinnikova, G.V., Kuznetzov, A.B., Melezhik, V.A., Gorokhov, I.M., Vasil'eva, I.M.,
816   Gorokhovsky, B.M., 2007. Pb-Pb age of Jatulian carbonate rocks: the Tulomozero Formation in
817   south-eastern Karelia. Stratigraphy and Geological Correlation 4, 359–372.
818
819   Qu, Y., Črne, A.E., Lepland, A., van Zuilen, M., 2012. Methanotrophy in a Paleoproterozoic oil
820   field ecosystem, Zaonega Formation, Karelia, Russia. Geobiology 10, 467–478.
821
822   Puchtel, I.S., Arndt, N.T., Hofmann, A.W., Haase, K.M., Kroner, A., Kulikov, V.S., Kulikova,
823   V.V., Garbe-Schonberg, C.D., Nemchin, A.A., 1998. Petrology of mafic lavas within the Onega
824   plateau, central Karelia: evidence for 2.0 Ga plume-related continental crustal growth in the
825   Baltic Shield. Contributions to Mineralogy and Petrology 130, 134–153, doi:
826   10.1007/s004100050355.
827   Puchtel, I.S., Brugmann, G.E., Hofmann, A.W., 1999. Precise Re-Os mineral isochron and Pb-
828   Nd-Os isotope systematics of a mafic-ultramafic sill in the 2.0 Ga Onega plateau (Baltic Shield):
829   Earth and Planetary Science Letters 170, 447–461, doi: 10.1016/S0012-821X(99)00118-1.
830
831   Reuschel, M., Melezhik, V.A., Strauss, H., 2012. Sulfur isotopic trends and iron speciation from
832   the c. 2.0 Ga Pilgujarvi Sedimentary Formation, NW Russia. Precambrian Research 196, 193–
833   203, doi: 10.1016/j.precamres.2011.12.009.
834
835   Schidlowski, M., 2001. Carbon isotopes as biogeochemical recorders of life over 3.8 Ga of Earth
836   history: evolution of a concept. Precambrian Research 106, 117–134.
837
838   Shatsky, G.V. 1990. Isotope composition of sulphides from the Zazhogino shungite deposit.
839   Lithology and Mineral Resources 1, 20–28. (in Russian)
840
841   Shieh, Y.M., Taylor, H.P., 1969. Oxygen and carbon isotope studied of contact metamorphism of
842   carbonate rocks. Journal of Petrology 10, 307–331.
843
844   Strauss, H., Melezhik, V.A., Lepland, A., Fallick, A.E., Hanski, E.J., Filippov, M.M., Deines,
845   Y.E., Illing, C.J., Črne, A.E., Brasier, A.T., 2013. 7.6 Enhanced Accumulation of Organic
846   Matter: The Shunga Event. In: Melezhik, V.A., Kump, L.R., Fallick, A.E., Strauss, H., Hanski,
847   E., Prave, A.R., Lepland, A., (Eds.), Reading the Archive of Earth's Oxygenation, vol. 3,
848   Springer, pp. 1195–1273.
849
850   Valley, J.W., 1986. Stable isotope geochemistry of metamorphic rocks. In: Valley, J.W., Taylor,
851   H.P., O'Neil, J.R. (Eds.), Stable Isotopes in High Temperature Geological Processes. Reviews in
852   Mineralogy 16, Mineralogical Society of America, pp. 445–490.
853
854   Volodichev, O.I., 1987. Metamorphism. In: Sokolov, V.A. (Eds.), Geology of Karelia, Nauka,
855   Leningrad, pp. 152–175. (in Russian)
856
857   Whiticar, M.J., 1999. Carbon and hydrogen isotope systematics of bacterial formation and
858   oxidation of methane. Chemical Geology 161, 291–314.
859

860   Yudovich, Y.E., Makarikhin, V.V., Medvedev, P.V., Sukhanov, N.V., 1991. Carbon isotope
861   anomalies in carbonates of the Karelian Complex. Geochemica International 28, 56–62.

862 **Figure captions**
863 **Fig. 1.** Geological map of the Lake Onega area in central Karelia showing locations of the FAR-
864 DEEP drillholes that targeted the Zaonega Formation. The Tulomozero Formation preserves the
865 Lomagundi-Jatuli isotopic signal.

866 **Fig. 2.** Lithostratigraphic columns of the FAR-DEEP drillholes 12AB and 13A (after Črne et al.,
867 2013a,b) with marked stratigraphic positions of the carbonate beds selected for this study.

868 **Fig. 3.** Selected carbonate beds with lithological information and geochemical parameters. Beds
869 #1 and #2 are from drillhole 13A; beds #3 to #8 are from drillhole 12AB.

870 **Fig. 4.** Carbon and oxygen isotope profiles of carbonate beds #1 to #7.

871 **Fig. 5.** SEM-BSE and CL images of samples from the centres (left column) and margins (right
872 column) of carbonate beds #2 to #5 from drillholes 13A and 12AB. All scale bars show 100 μm.
873 (a) SEM-BSE image of large dolomite crystals, as much as 20 μm in size, which are zoned and
874 tightly intergrown. Overgrowing the dolomite are calcite, mica and talc; calcite occurs as
875 irregular patches of different size (centre of bed #2; sample 13A-144.27 m). (b) SEM-BSE image
876 showing calcite containing a few μm-scale rounded intercalations of quartz (marked by white
877 arrows). Also present are pyrite grains, partly overgrown by calcite. Mica is overgrowing both
878 calcite and pyrite (margin of bed #2; sample 13A-144.39 m). (c) CL image showing bright and
879 dull red luminescence of calcite (margin of bed #2; sample 144.39 m). (d) SEM-BSE image of
880 dolomite rhombohedra as large as 20 μm, which are zoned and tightly intergrown. Quartz is
881 present as dark, irregular patches in places overgrown by calcite containing spherical
882 intercalations of quartz. Calcite, mica and pyrite overgrow the dolomite (centre of bed #3;
883 sample 12B-126.88 m). (e) Large, irregular patches of calcite containing spherical intercalations
884 of quartz are overgrowing the quartz-mica matrix. Small, irregular grains of pyrite are
885 disseminated throughout the sample (margin of bed #3; sample 12B-126.52 m). (f) CL image
886 showing red luminescence of calcite, whereas dolomite, micas and pyrite are non-luminescent
887 (centre of bed #3; sample 12B-126.88 m). (g) Homogenous dolomite rhombohedra overgrown by
888 mica and calcite, the latter containing intercalations of quartz (centre of bed #4; sample 12B-
889 162.99 m). (h) Calcite, with spherical intercalations of albite (marked by white arrows),
890 overgrowing mica. Large either rectangular or irregular patches of albite overgrow mica and
891 calcite. Pyrite is present as small grains and large cubes, the latter overgrowing mica, calcite and
892 albite (margin of bed #4; sample 12B-163.13 m). (i) CL image of dull to bright red luminescent
893 calcite and dark, non-luminescent pyrite, mica and albite (margin of bed #4; sample 12B-163.13
894 m). (j) SEM-BSE image of zoned dolomite rhombohedra cemented together by dolomite cement
895 and in places surrounded by organic-matter (black) (centre of bed #5; sample 12B-183.4 m). (k)
896 SEM-BSE image of dolomite rhombohedra composed of a dark core and a bright rim, cemented
897 by large amount of homogenous dolomite cement. Some calcite containing intercalations of
898 quartz is overgrowing the dolomite. Mica overgrows both, dolomite and calcite (margin of bed
899 #5; sample 12B- 183.11 m). (l) CL image showing mostly red luminescence of rims of the

900 dolomite rhombohedra, but also some luminescent cores. The bulk of the dolomite is non-
901 luminescent (centre of bed #5; sample 12B-183.4 m).

902 **Fig. 6.** SEM-BSE and CL images of samples from the centres (left column) and margins (right
903 column) of carbonate beds #1 from drillhole 13A and #6 from drillhole 12AB. All scale bars
904 show 100 μm. (a) SEM-BSE image of mostly homogenous dolomite crystals, which are tightly
905 intergrown, with straight boundaries between the crystals. Margins of the dolomite crystals are
906 slightly brighter than the crystal cores. Minor amounts of calcite and mica are present, calcite
907 mostly occurring as irregular patches (centre of bed #1; sample 13A-58.16 m). (b) SEM-BSE
908 image of rhombohedral dolomite crystals, mostly tightly intergrown with straight contacts, but
909 also loosely packed and surrounded by organic-matter (black). A few irregular calcite patches are
910 present either overgrowing dolomite rhombohedra (lower right part of the photo) or as
911 precipitates along the dolomite crystal boundaries (margin of bed #1; sample 13A-58.45 m). (c)
912 CL image showing dull red luminescence of dolomite crystals and some bright red luminescence
913 of crystal-margins (centre of bed #1; sample 58.16 m). (d) CL image of dolomite with dull and
914 bright red zones (margin of bed #1; sample 58.45 m). (e) SEM-BSE image of homogenous
915 dolomite crystals, very tightly intergrown as indicated by sutured crystal boundaries,
916 recognizable due to their darker colour. Some mica and a few small patches of calcite are
917 present, calcite mostly along the dolomite crystals but clearly overgrowing dolomite (centre of
918 bed #6; sample 12B-249.5). (f) SEM-BSE image of quartz-rich sample containing patches of
919 calcite with spherical intercalations of quartz (margin of bed #6; sample 12B-248.7 m).

920 **Fig. 7.** SEM-BSE and CL images of samples from the centres (left column) and margins (right
921 column) of carbonate beds #7 to #8 from drillhole 12AB. All scale bars show 100 μm. (a) SEM-
922 BSE image of calcite consisting of homogenous crystals of various shapes and as much as 30 μm
923 in size, in places rhombohedra can be recognized. Albite occurs mostly as rectangular grains
924 (?replacing pyrite) but also as small intercalations of spherical shape. Some mica and small
925 titanite crystals are also present (centre of bed #7; sample 12B-283.02 m). (b) Up to 0.5 cm large
926 rhombohedra are composed of calcitic core and calcitic rim, the boundaries between the two are
927 marked by spherical intercalations of quartz; rhombohedra cores contain intercalations of albite
928 (margin of bed #7; sample 12B-282.65 m). (c) CL image of dull red to bright red luminescent
929 calcite and nonluminescent albite (centre of bed #8; sample 12B-283.02 m). (d) SEM-BSE image
930 of large, irregular calcite patches having undulating contacts with surrounding albite. Much mica
931 and some titanite are also present. Actinolite needles overgrow all minerals phases (margin of
932 bed #8; sample 12B-394.30 m).

933 **Fig. 8.** (a) Cross-plotted values of $\delta^{13}C$ and Mg/Ca ratio with separate symbols for each of the
934 studied beds. (b) Cross-plotted values of $\delta^{13}C$ and (Mg/Ca)*IC, a product between the Mg/Ca
935 ratio and inorganic carbon (IC) content, with separate symbols for each of the studied beds. Also
936 plotted are data points for samples analysed for $\delta^{13}C$ by Kump et al. (2011). Thresholds of
937 (Mg/Ca)*IC are used for approximation of sample alteration. (c) Cross-plotted values of $\delta^{13}C$
938 and IC with separate symbols for each of the studied beds. (d) Cross-plotted values of $\delta^{13}C$ and

939    $\delta^{18}O$ with separate symbols for each of the studied beds. The two minor to moderately altered
940   samples from Kump et al. (2011), recognized on the basis of (Mg/Ca)*IC (Fig. 9b), are also
941   plotted. The $\delta^{13}C$ vs. $\delta^{18}O$ alteration trends for the samples located in the two beds, which
942   contain minor to moderately altered samples, are parallel and indicated by the thick grey arrows.
943   The line cutting off the least altered samples, on the basis of the data presented, is oriented
944   perpendicular to the $\delta^{13}C$ vs. $\delta^{18}O$ alteration trend.

945   **Fig. 9.** $\delta^{13}C$ and $\delta^{18}O$ values of samples from this study and the study of Kump et al. (2011)
946   plotted along the combined lithostratigraphic column of drillholes 12AB and 13A. The samples
947   are divided into four groups with different alteration grades, which correspond to the amount of
948   dolomite within the sample. The least altered carbonate samples have the largest symbols with a
949   thick black line and are denoted with an asterisk.

950